Magmatic immiscibility and the origin of magnetite-(apatite) iron deposits

Dorota K. Pietruszka
Memorial University of Newfoundland
John M. Hanchar (jhanchar@mun.ca)
Memorial University of Newfoundland
Fernando Tornos
Instituto de Geociencias (CSIC-UCM)
Richard Wirth
GFZ German Research Centre for Geosciences
Nathan A. Graham
University of Alaska Fairbanks
Kenneth P. Severin
University of Alaska Fairbanks
Francisco Velasco
Universidad del País Vasco UPV/EHU
Matthew Steele-MacInnis
University of Alberta
Wyatt M. Bain
Lakehead University

Research Article

Keywords: magnetite-(apatite) deposit, melt immiscibility

Posted Date: October 12th, 2022

DOI: https://doi.org/10.21203/rs.3.rs-2156064/v1

Magmatic immiscibility and the origin of magnetite-(apatite) iron deposits

Dorota K. Pietruszka[1], John M. Hanchar[1*], Fernando Tornos[1,2], Richard Wirth[3], Nathan A. Graham[4], Kenneth P. Severin[4], Francisco Velasco[5], Matthew Steele-MacInnis[6], Wyatt M. Bain[7]

[1]Department of Earth Sciences, Memorial University of Newfoundland; St. John's, NL A1B 3X5 Canada.

[2]Instituto de Geociencias (CSIC-UCM); Severo Ochoa 7, 28040 Madrid, Spain.

[3]GFZ German Research Centre for Geosciences, Section 3.5 Interface Geochemistry; Telegrafenberg, Potsdam 14473, Germany.

[4]Department of Geosciences, University of Alaska Fairbanks; Fairbanks, AK 99775, USA.

[5]Departamento de Mineralogía y Petrología, Universidad del País Vasco UPV/EHU; 48080 Bilbao, Spain.

[6]Department of Earth & Atmospheric Sciences, University of Alberta; Edmonton, AB T6G2E3, Canada.

[7]Department of Geology, Lakehead University; Thunder Bay, ON P7B 5E1, Canada.

*Corresponding author. Email: jhanchar@mun.ca

Abstract

The origin of magnetite-(apatite) iron deposits (MtAp) is among the most contentious issue in ore geology with competing models involving purely hydrothermal to magmatic processes. We study here melt inclusions trapped in plagioclase phenocrysts in andesite hosting the emblematic MtAp mineralization at El Laco, Chile. Our high-resolution study reveals that individual melt inclusions preserve complex processes of melt immiscibility including the separation of Si- and Fe-rich melts, the latter hosting other Cu-sulfide, phosphate-rich, and C-O-HFSE-rich residual melts. This assemblage is a small-scale analogue of the ore mineralization and establishes the missing link between silicate and Fe-P-rich melts which subsequently produce extrusive magnetite. These results strongly indicate that El Laco mineralization derives from

crystallization of Fe-P-rich melts providing insight into the formation of similar deposits elsewhere.

Main Text

The El Laco volcanic complex (ELVC) in the Central Volcanic Zone (CVZ) in northern Chile (Fig. 1), hosts bodies of enigmatic magnetite-(apatite) (MtAp) iron mineralization. El Laco is one of the youngest examples on Earth of MtAp mineralization with pristine outcrop exposure, an excellent drill core record, and as such this single locality has been at the focus of one of the most vigorous debates in the history of ore deposits. The genesis of this massive magnetite mineralization that resembles lava flows and related feeder dykes remains unclear despite numerous studies for six decades[1–4]. Even today there is no consensus on how MtAp deposits form[1,5–10], whether they are an independent style of mineralization, or genetically related to other systems, like iron oxide-copper-gold deposits (IOCG)[5,11]. Yet, these Paleoproterozoic to Holocene deposits are a significant source of iron in Chile, China, Iran, Peru, and Sweden, and have significant resource for fluorite, REE, cobalt, and phosphorus[5,11].

The ELVC shows strong crustal radiogenic isotope signatures[12–14] and has been dated (K-Ar) between 5.3±1.9 and 1.6±0.5 Ma[15]. Plagioclase and clinopyroxene phenocrysts in the ELVC andesite host numerous melt inclusions that have textures with contrasting compositions indicating immiscibility between Fe-rich and Si-rich melts. These melt inclusions have previously been investigated[16,17], but never at high-resolution. This and other widespread geologic and geochemical evidence at El Laco, led some previous researchers to propose that the magnetite mineralization was the product of the crystallization of an unusual Fe-rich melt[1,3,4,18,19] that was accompanied by exsolution of hydrothermal fluids leading to pervasive metasomatic alteration of the host rocks[8,14,17]. Other researchers have proposed alternative genetic hypotheses including: 1) metasomatic replacement of host andesite by hydrothermal fluids of either basinal or magmatic-hydrothermal derivation[2,6,10]; or 2) ascent of magmatic magnetite via flotation facilitated by attached fluid-solid aggregates with deposition due to decompression[7,20].

We present results of a high-resolution study of melt inclusions at the nanometer scale entrapped in plagioclase phenocrysts from three andesite samples at El Laco that hosts the MtAp mineralization (Fig. 1, S1). We present new data on microtextures, chemical compositions, and phase proportions of crystallized immiscible melts preserved in melt inclusions, and also the temperature of homogenization and the chemical composition of the parental melt. Results were obtained using high-resolution transmission electron microscopy (HR-TEM), a field emission gun-electron probe microanalyzer (FEG-EPMA), microthermometry, Raman spectroscopy, and EPMA (see Methods section). Our results reveal the unexpectedly complex nature of melt immiscibility during the magmatic evolution of the El Laco system and illuminate how immiscibility drives MtAp mineralization.

Results of melt inclusion study

The melt inclusions comprise two main contrasting phases; clinopyroxene (cpx) and magnetite (mt) globules (1-6μm in diameter), which are enclosed in a high-Si, Al-K-Na dacite glass (Fig. 2-3a, S2). The cpx-mt globules are interpreted to be the crystallized product of an Fe-rich melt (Fig. 4a) and are texturally similar to other natural samples recording Fe-rich and Si-rich immiscibility (e.g., [21]). We calculated the average compositions of these conjugate melts based on FEG-EPMA spot analyses (Table S1-S4). Phase proportions of the Fe-rich globules and high-SiO_2 dacite glass were estimated, on average, at 14 modal % (range: 5-30%) and 86 modal % (range: 70-95%), respectively (Table S5, Fig. 5a). The high-SiO_2 dacite glass also includes ~5 modal % of euhedral clinopyroxene crystals having low Ti and negligible P contents based on EDS analysis with HR-TEM (Fig. S2D, S3H-I, S4D). The high-SiO_2 dacite glass is partially devitrified and also hosts minor 150-300 nm globules of NaCl ± Fe-oxide (Figs. 3a, S2D-F) and anhedral K-feldspar crystals.

The spherical cpx-mt globules form a consistent phase assemblage of ~82 modal % clinopyroxene of augite-pigeonite composition with TiO_2 and P_2O_5 contents of 5.59 and 2.26 wt.%, respectively, and ~18 modal % of magnetite (Fig. S4C, S5; Table S1, S6). The anhedral clinopyroxene shows a "cauliflower-like" texture, with irregular shapes (Fig. 3a-b). Two types of magnetite are hosted by clinopyroxene within the globules: 1) subhedral to anhedral, elongate crystals 50-200 nm in diameter with longer crystallographic axis oriented outward from the center of the globule (Fig. 3a, c); and 2) euhedral crystals 150-400 nm in diameter that have grown on outer surfaces of the globules (Fig. S2A, C). The cpx-mt globules contain pores, especially abundant in the polycrystalline magnetite (Fig. 3a).

Some of the cpx-mt globules contain inner "cores", or nucleation sites, of subspherical 1-2 μm globules of predominantly Cu-S-rich composition (rarely Fe-Cu-S composition) that occur in come cases associated with nanoscale amorphous SiO_2. The morphology of these Cu-S globules varies from spherical to subspherical, with a partially curved meniscus at the interface with the clinopyroxene (Fig. 3a). The TEM electron diffraction peak indexing of the Cu-S phase matches that of digenite (Cu_9S_5; Fig. S3D-E). The FEG-EPMA analyses of the Cu-S show 64-74 wt.% Cu and 20-34 wt.% S, and the calculated stoichiometry indicates phase compositions between covellite and digenite (Table S7-8). The concentration of Cu in the cpx-mt globules (where the Cu-S phase has been observed) was calculated to be as high as 10.6 wt.% with a Cu/Fe ratio of 0.32 as estimated from the volume proportions and chemical compositions (Table S9, Fig. S6).

Rarely, the cpx-mt globules contain <2 μm^2 of subhedral fluorapatite that occupies ~5 modal % of the area of cpx-mt globules (Fig. 3d, S3A; Table S10). Larger euhedral and smaller anhedral magnetite crystals are associated solely with clinopyroxene and not fluorapatite. Both fluorapatite and clinopyroxene contain multiple solid inclusions having different compositions

and different crystal morphologies. The clinopyroxene contains Fe- and Ca-rich lamellae and hosts multiple inclusions of quartz. Several <250 nm, subhedral to euhedral, magnetite crystals with minor Ti, Mg, and Al are located at the edge of, or adjacent to, quartz inclusions (Fig. S3C). The clinopyroxene in the cpx-mt globules also contain droplets of a phosphate melt crystallized to apatite. The fluorapatite hosts regularly distributed and abundant, <100 nm, spherical nanoscale melt inclusions composed of C-Si-Cl-Al-rich glass with daughter crystals of ilmenite with Th-Nb-Y-U-Zr (confirmed by TEM-EDS and electron diffraction patterns; Fig. 3e, S3L-M, S4G-H). To our knowledge, this is the first reporting ever of melt inclusions occurring within a crystal inside another melt inclusion at the nm scale. The fluorapatite also hosts: 1) rare, individual Ca-phosphate REE-C-rich Si-F-S nanoscale crystals; 2) Si-O-Cl-Fe-Ti melt inclusions; and 3) solid NaCl inclusions. The modal proportion of these nanoscale melt inclusions in the fluorapatite is ~13% (Table S10). The presence of phosphate inclusions in the clinopyroxene and silicate inclusions in apatite suggests coeval, but separate crystallization.

During heating experiments to homogenize the melt inclusions, the cpx-mt globules progressively dissolved between 900°C and 1145°C (see Supplementary Text in Supplementary information) showing that the immiscibility process recorded in the melt inclusions is reversable to a single-phase state as in any equilibrium process. The vapor bubbles that remained undissolved have equal molar proportions of CO_2 and SO_2 (Fig. S7-S8). To our knowledge, these vapor bubbles are the most SO_2-rich vapor bubbles ever reported in melt inclusion study. The average composition of the homogenized melt inclusions (Fig. S9; Table S1, S11) varies around the average composition of dacite and is more felsic than the andesite from the ELVC (Fig. 5b-c).

Polyphase immiscibility in the formation of El Laco deposit

The individual melt inclusions record a small-scale complex evolution of magma immiscibility by which the different melts separated from each other during cooling. The distinct compositions and curved menisci of the cpx-mt globules in high-SiO_2 dacite glass, the Cu-S globules in cpx-mt globules, and the C-O-Si-Cl-Al-HFSE nanoscale melt inclusions in fluorapatite (Fig. 2-3), strongly suggests the presence of multiple, complex, interconnected, and immiscible liquids: Fe-rich, Si-rich, sulfide-rich, phosphate-rich, and residual C-O-Si-Cl-Al-HFSE-rich. The abundance of immiscible globules, their variable sizes within and among multiple melt inclusions, with consistent phase proportions and chemical compositions, strongly suggests that these solid droplets represent primary, immiscible melts[22].

Our interpretation is that the magmatic system initiates with the separation of conjugate Fe-rich (i.e., Fe-Mg-Ca-P-Ti-F-Cu-S-C-O-Cl-HFSE) and Si-rich (i.e., Si-Al-K-Na-O) melts from a crustally contaminated, parental calc-alkaline melt[12,14]. Elemental distribution of these Fe- and Si-rich immiscible melts agrees, within limitations of analytical uncertainty, with the fractionation of elements between Fe- and Si-rich melts reported in the studies of both experimental and natural samples (Fig. 4;[23–26]). After separation, the Fe-rich melt eventually crystallizes as clinopyroxene and magnetite. Experiments have shown that Cu and S partition preferentially into the Fe-rich phase[24,27], and that the addition of <3 wt.% of S into a silicate liquid of intermediate composition (± H_2O, P, F) at 1000-1200°C stabilizes a third immiscible sulfide liquid[25,26]. In these experiments, the sulfide melt formed a sphere within the globule of immiscible Fe-rich melt embedded in the Si-rich melt[25]. Those textures and phase relationships are remarkably similar to those reported in the present study (Fig. 3a), and suggest that the formation of an immiscible sulfide liquid is closely related to the Fe-rich melt. Typical magmatic sulfides, however, have much lower Cu/Fe ratios (e.g., pyrrhotite, chalcopyrite) than the sulfide

melt that crystallized in these melt inclusions (≤1 vs >60, respectively). Experimental studies have shown that the last sulfide phase formed before S transition from the sulfide to sulfate state (at NNO +1 fO_2[28]) is a Cu-rich sulfide (e.g., chalcocite Cu_2S) that can coexist in equilibrium with anhydrite at sub-magmatic temperatures[29]. Also, recent studies show that an increase of redox buffer causes the transition from reduced S-rich immiscible melt to Ca-S-O melt in the presence of immiscible P-Fe-rich melt[30]. The presence of the observed magnetite and digenite assemblage strongly suggests that the system overall formed under high fO_2-fS_2 conditions, probably close to the hematite-magnetite and covellite-digenite phase boundaries[31].

In our model, as the system cooled, a final phosphate-C-O-Si-Cl-Al-HFSE melt separated from the Fe-rich melt. Crystallization of fluorapatite then produced a final residual melt enriched in incompatible elements that is represented by the nanoscale melt inclusions containing the carbonates, ilmenite, halite and other chlorides, and minor SiO_2. We have not observed anhydrite within the melt inclusions, but anhydrite has been described in similar melt inclusions in andesite from El Laco[16,17], suggesting that sulfate was also a significant component in this magmatic system. Also, droplets of a phosphate-rich melt (i.e., fluorapatite with curved menisci) in the silica-rich glass of melt inclusions have previously been reported from pyroxene phenocrysts in the ELVC andesite[17]. Despite the lack of direct evidence for the presence of liquid water, the plagioclase hosting the melt inclusions has albitized aureoles and the cpx-mt globules contain multiple pores that suggests the presence of an aqueous phase exsolved during cooling from the crystallizing melts[17] (Fig. 2a, 3a).

Our results point to a direct, parallel relationship between the evolution recorded by melt inclusions at the nanoscale, and the formation of MtAp deposits at the macroscale (Fig. 6). The dominant mineral assemblage is the same and includes magnetite, Ca-Fe-rich pyroxene, fluorapatite, and anhydrite. This phase assemblage is consistent with an early formation of a

magnetite-rich body with later crystallization of clinopyroxene and fluorapatite, that can form pegmatite-like bodies composed of Ca-Mg silicates, fluorapatite (commonly with inclusions of monazite), and variable amounts of magnetite, ilmenite, and anhydrite[14]. The latter result is similar to a recent study[19] that showed that apatite, actinolite, and magnetite from MtAp ore bodies at the Buena Vista (Nevada, USA) and Iron Springs deposits (Utah, USA) host carbonate-sulfate-Fe-rich melt inclusions resembling the final, residual melt found in the El Laco samples reported in the present study. Fe-sulfate-rich melt is also present in the inclusions from the late ore-stage diopside-magnetite-anhydrite veins at El Laco[32]. Except for the large accumulations of anhydrite at El Laco[14], the residual carbonate-sulfate melts or silica-rich droplets do not form stable mesoscopic assemblages. Additionally, in intrusive MtAp systems fluorapatite forms large massive bodies that typically cap the magnetite ore which supports its late crystallization[9,14]. The results presented here are also consistent with the presence of immiscible Fe-P-S-O melts observed at El Laco[3,33] and with experiments that report phosphate-rich immiscible melts that had separated from an Fe-rich melt[3,30].

We advocate that the key process that initiated the formation of the Si-depleted, Fe-P-S-C-O-HFSE-rich melt, key to forming MtAp mineralization, is crustal assimilation by the ascending andesite. The host ELVC andesite has highly radiogenic Sr isotopes values[14] indicating significant interaction of primitive melts with crustal components[12,13]. The MtAp ore has higher radiogenic crustal values ($^{87}Sr/^{86}Sr$ 0.7083) than the andesite ($^{87}Sr/^{86}Sr$ 0.7066–0.7074), which has been interpreted as reflecting varying degrees of assimilation of continental rocks by the primitive melts at depths greater than 1-2 km. Potential crustal contaminants include the evaporites and carbonates of the Salta Group[14,34] and/or P-rich oolitic ironstone and coquinas of Ordovician-Devonian age[14,35] that underlie the ELVC. Experimental studies and phase

equilibria modeling[3,30] have shown, that the elevated P, S, and F concentrations, and an oxidized environment (higher fO_2), expand the miscibility gap for Fe-rich and Si-rich melts[25].

The average 40 wt.% SiO_2 of the cpx-mt globules indicate high values of coefficient D that describes SiO_2 partitioning between conjugate Fe-rich and Si-rich melts (av. 0.59 $D_{SiO2}^{LFe/LSi}$; Fig. 4b; see [23,26]). As stated in recent study[14], these melt inclusions containing globules of clinopyroxene greater than magnetite are probably not strictly the parental melt from which the magnetite ore crystallized, but their poorly-contaminated analogue. Only magmas that experienced a greater degree of crustal contamination and, thus, with $D_{SiO2}^{LFe/LSi}$ values as low as 0.2-0.3, can form low-SiO_2 melts[23,26]. Both melts behave similarly but only the latter, with high Fe/Si ratios, have a viscosity low enough to be able to coalesce, ascend, and form MtAp mineralization like that found at El Laco.

Our micro- and nano-scale study shows that multiple interconnected immiscible melts controlled by fO_2 can produce macro-scale MtAp mineralization, and similarities of the El Laco system with other MtAp deposits suggest that analogous processes can lead to the formation of MtAp mineralization worldwide. Furthermore, our study has implications beyond genesis of MtAp mineralization. The formation of Fe-O melts that later form massive magnetite inhibit the formation of Fe-Cu-S melts, as Cu sequesters the small amounts of available reduced sulfur, which later transform to the sulfate state. In less oxidized calc-alkaline arc magmas (fO_2 <NNO+1), any Cu stored in the immiscible Cu-sulfide melt could lead to the formation of Cu-rich porphyry mineralization. 100 km south of El Laco, broadly coeval highly oxidized Cu-Au porphyry systems contain Cu-rich sulfides with abundant anhydrite and magnetite (e.g., Arizaro, Lindero[36]), which could reflect re-dissolution of this Cu-rich precursor and its further precipitation in a magmatic-hydrothermal system in a process similar to that described by [37] at the slightly older (~7 Ma) Bajo de Alumbrera porphyry copper deposit. Moreover, the Cu

contained in the immiscible sulfide melt could supply this metal for coeval or later superimposed iron oxide-copper-gold (IOCG) mineralization.

References and Notes:

1. Park, F. A magnetite 'flow' in northern Chile. *Econ. Geol.* **56**, 431–436 (1961).

2. Sillitoe, R. H. & Burrows, D. R. New field evidence bearing on the origin of the El Laco magnetite deposit, Northern Chile. *Econ. Geol.* **97**, 1101–1109 (2002).

3. Mungall, J. E., Long, K., Brenan, J. M., Smythe, D. & Naslund, H. R. Immiscible shoshonitic and Fe-P-oxide melts preserved in unconsolidated tephra at El Laco volcano, Chile. *Geology* **46**, 255–258 (2018).

4. Henriquez, F. & Martin, R. F. Crystal growth textures in magnetite flows and feeder dykes, El Laco, Chile. *Can. Mineral.* **16**, 581–589 (1978).

5. Hitzman, M. W., Oreskes, N. & Einaudi, M. T. Geological characteristics and tectonic setting of proterozoic iron oxide (Cu-U-Au-REE) deposits. *Precambrian Res.* **58**, 241–287 (1992).

6. Barton, M. D. & Johnson, D. A. Evaporitic-source model for igneous-related Fe oxide-(REE-Cu-Au-U) mineralization. *Geology* **23**, 259–262 (1996).

7. Knipping, J. L. *et al.* Giant Kiruna-type deposits form by efficient flotation of magmatic magnetite suspensions. *Geology* **43**, 591–594 (2015).

8. Tornos, F., Velasco, F. & Hanchar, J. M. Iron-rich melts, magmatic magnetite, and superheated hydrothermal systems: The El Laco deposit, Chile. *Geology* **44**, 427–430 (2016).

9. Tornos, F., Hanchar, J. M., Munizaga, R., Velasco, F. & Galindo, C. The role of the subducting slab and melt crystallization in the formation of magnetite-(apatite) systems, Coastal Cordillera of Chile. *Miner. Depos.* **56**, 253–278 (2020).

10. Dare, S. A. S., Barnes, S. J. & Beaudoin, G. Did the massive magnetite "lava flows" of El Laco (Chile) form by magmatic or hydrothermal processes? New constraints from magnetite composition by LA-ICP-MS. *Miner. Depos.* **50**, 607–617 (2015).

11. Groves, D. I., Bierlein, F. P., Mainert, L. D. & Hitzman, M. W. Iron Oxide Copper-Gold (IOCG) Deposits through Earth history: implications for origin, lithospheric setting, and distinction from other epigenetic Iron Oxide Deposits. *Econ. Geol.* **105**, 641–654 (2010).

12. Harmon, R. S. *et al.* Regional O-, Sr-, and Pb-isotope relationships in Late Cenozoic calc-alkaline lavas of the Andean Cordillera. *Geol. Soc. London* **141**, 803–822 (1984).

13. Mamani, M., Tassara, A. & Wörner, G. Composition and structural control of crustal domains in the central Andes. *Geochemistry, Geophys. Geosystems* **9**, (2008).

14. Tornos, F., Velasco, F. & Hanchar, J. M. The magmatic to magmatic-hydrothermal evolution of the El Laco deposit (Chile) and its implications for the genesis of magnetite-apatite deposits. *Econ. Geol.* **112**, 1595–1628 (2017).

15. Naranjo, J. A., Henríquez, F. & Nyström, J. O. Subvolcanic contact metasomatism at El Laco Volcanic Complex , Central Andes. *Andean Geol.* **37**, 110–120 (2010).

16. Naslund, H. R. *et al.* Melt inclusions in silicate lavas and iron-oxide tephra of the El Laco vocano, Chile. In *XII Congreso Geológico Chileno,* 1–4 (2009).

17. Velasco, F., Tornos, F. & Hanchar, J. M. Immiscible iron- and silica-rich melts and magnetite geochemistry at the El Laco volcano (northern Chile): Evidence for a magmatic

origin for the magnetite deposits. *Ore Geol. Rev.* **79**, 346–366 (2016).

18. Naslund, H. R., Henríquez, F., Nyström, J. O., Vivallo, W. & Dobbs, F. M. Magmatic iron ores and associated mineralization: examples from the Chilean High Andes and Coastal Cordillera. In *Hydrothermal Iron Oxide Copper-Gold and Related Deposits: A Global Perspective, v. 2* (ed. Porter, T. M.), 207–226 (PGC Publishing, 2002).

19. Bain, W. M. *et al.* A fundamental role of carbonate–sulfate melts in the formation of iron oxide–apatite deposits. *Nat. Geosci.* **23**, 751–757 (2020).

20. Ovalle, J. T. *et al.* Formation of massive iron deposits linked to explosive volcanic eruptions. *Sci. Rep.* **8**, 1–11 (2018).

21. Kontak, D. J., De Wolfe De Young, M. Y. & Dostal, J. Late-stage crystallization history of the Jurassic North Mountain Basalt, Nova Scotia, Canada. I. Textural and chemical evidence for pervasive development of silicate-liquid immiscibility. *Can. Mineral.* **40**, 1287–1311 (2002).

22. Frezzotti, M. Silicate-melt inclusions in magmatic rocks: applications to petrology. *Lithos* **55**, 273–299 (2001).

23. Kamenetsky, V. S. *et al.* Magma chamber-scale liquid immiscibility in the siberian traps represented by melt pools in native iron. *Geology* **41**, 1091–1094 (2013).

24. Lester, G. W., Kyser, T. K., Clark, A. H. & Layton-Mathews, D. Trace element partitioning between immiscible silicate melts with H_2O, P, S, F, and Cl. *Chem. Geol.* **357**, 178–185 (2013).

25. Lester, G. W., Clark, A. H., Kyser, T. K. & Naslund, H. R. Experiments on liquid immiscibility in silicate melts with H_2O, P, S, F and Cl: Implications for natural magmas.

Contrib. to Mineral. Petrol. **166**, 329–349 (2013).

26. Hou, T. *et al.* Immiscible hydrous Fe-Ca-P melt and the origin of iron oxide-apatite ore deposits. *Nat. Commun.* **9**, 1–8 (2018).

27. Veksler, I. V., Dorfman, A. M., Danyushevsky, L. V., Jakobsen, J. K. & Dingwell, D. B. Immiscible silicate liquid partition coefficients: Implications for crystal-melt element partitioning and basalt petrogenesis. *Contrib. to Mineral. Petrol.* **152**, 685–702 (2006).

28. Carroll, M. R. & Rutherford, M. J. Sulphide and sulfate saturation in hydrous silicate melts. *J. Geophys. Res.* **90**, C601–C612 (1999).

29. Wohlgemuth-Ueberwasser, C. C., Fonseca, R. O. C., Ballhaus, C. & Berndt, J. Sulfide oxidation as a process for the formation of copper-rich magmatic sulfides. *Miner. Depos.* **48**, 115–127 (2013).

30. Lledo, H. L., Naslund, H. R. & Jenkins, D. M. Experiments on phosphate – silicate liquid immiscibility with potential links to iron oxide apatite and nelsonite deposits. *Contrib. to Mineral. Petrol.* **175**, 1–33 (2020).

31. Barton, P. B. J. & Skinner, B. J. Sulfide mineral stabilities. In *Geochemistry of Hydrothermal Ore Deposits* (ed. Barnes, H. L.), 278–403 (Wiley–Interscience, 1979).

32. Bain, W. M. *et al.* Evidence for iron-rich sulfate melt during magnetite(-apatite) mineralization at El Laco, Chile. *Geology* **49**, 1044–1048 (2021).

33. de Fourestier, J. F. Application of ATLAS 5 large-area and nano-scale imaging to purported volcanic products of the El Laco volcano, Chile. (Carleton University, 2019).

34. Matthews, S. J., Marquillas, R. A. & Kemp, A. J. The lateral extent of the Yacoraite formation (Maastrichtian) beneath the Tertiary-recent volcanic deposits of the NE Chile

and NW Argentina at 23°S. In *VIII Congreso Geologico Chileno*, 534–538 (1997).

35. Boso, M. A. & Monaldi, C. R. Oolitic stratabound iron ores in the Silurian of Argentina and Bolivia. *Soc. Geol. Appl. to Miner. Depos. Spec. Publ.* **8**, 175–186 (1990).

36. Simón, V. *et al.* Geology, geochemistry and geochronology of Lindero porphyry gold deposit in the Southern Puna plateau, Argentina. *J. South Am. Earth Sci.* **105**, (2021).

37. Halter, W. E., Pettke, T. & Heinrich, C. A. The origin of Cu/Au ratios in porphyry-type ore deposits. *Science* **296**, 1844–1846 (2002).

38. Honour, V. C., Holness, M. B., Partridge, J. L. & Charlier, B. Microstructural evolution of silicate immiscible liquids in ferrobasalts. *Contrib. to Mineral. Petrol.* **174**, 1–24 (2019).

39. Philpotts, A. R. Liquid immiscibility in silicate melt inclusions in plagioclase phenocrysts. *Bull. Minéralogie* **104**, 317–324 (1981).

40. Visser, W. & Koster van Gross, F. Effect of pressure on liquid immiscibility in the system K_2O-FeO-Al_2O_3-SiO_2-P_2O_5. *Am. J. Sci.* **279**, 1160–1175 (1979).

41. Best, M. G. Igneous and metamorphic petrology. (Blackwell Science, 2003).

Acknowledgments: We thank Compañía Minera del Pacífico (CMP), especially Rodrigo Munizaga, for logistic help access to the deposit, Anja Schreiber (GFZ Potsdam) for FIB sample preparation, Dr. Graham D. Layne for fruitful discussions, Drs. Michael Babechuk, Pedro Jugo, John Slack, Anthony E. Williams-Jones, Vadim S. Kamenetsky, Daniel J. Kontak, Stephen J. Piercey for informal review of our manuscript prior submission. **Funding:** This work was funded by a Natural Sciences and Engineering Research Council of Canada Discovery Grant to JMH (RGPIN/004649-2015) and by project RTI2018-099157-A-I00 (MCI/AEI/FEDER, UE) for FT and FV. **Author contributions:** FT, FV, and JMH conceived the project. FV and FT collected the samples. JMH, DKP, and FT conceptualized the project. JMH, RW, NG, KS, MS-M, WB, and DKP conducted data collection and curation. DKP synthesized and visualized the data and wrote the original manuscript. All authors contributed to review and approval of the final manuscript. **Competing interests:** Authors declare no competing interests. **Data and materials availability:** All data are available in the Supplementary Materials.

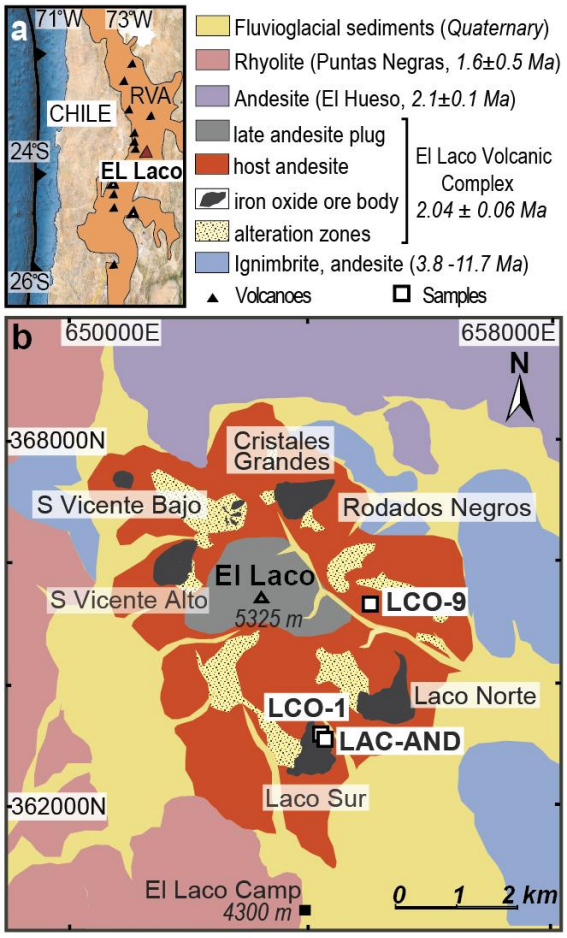

Fig. 1. Location of the El Laco MtAp deposit. (**a**) Regional location of El Laco deposit, Chile. RVA – recent volcanic arc. (**b**) Geological map of El Laco deposit with sample locations (modified from [8]).

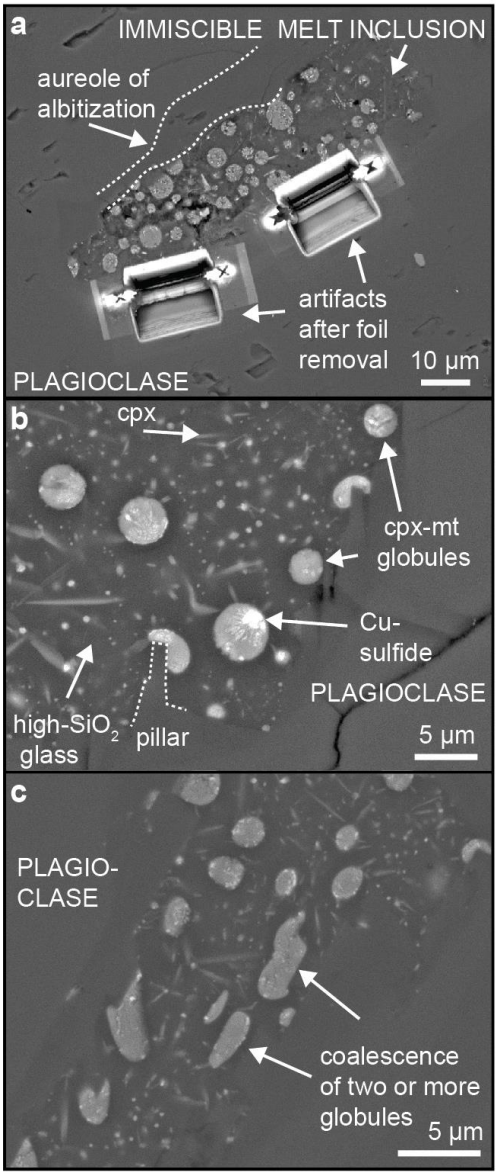

Fig. 2. Morphology of immiscible melt inclusions in plagioclase. (**a**) Melt inclusion with aureole of albitization. (**b**) Melt inclusion with immiscible clinopyroxene-magnetite globules (cpx-mt) and Cu-sulfide phase contained in high-SiO_2 dacite glass with euhedral clinopyroxene (cpx) crystals. Destabilized growth face of plagioclase by attached cpx-mt globule resulting in formation of pillar structure[38]. (**c**) Coalescence of cpx-mt globules. Scanning electron microscope back-scattered electron images.

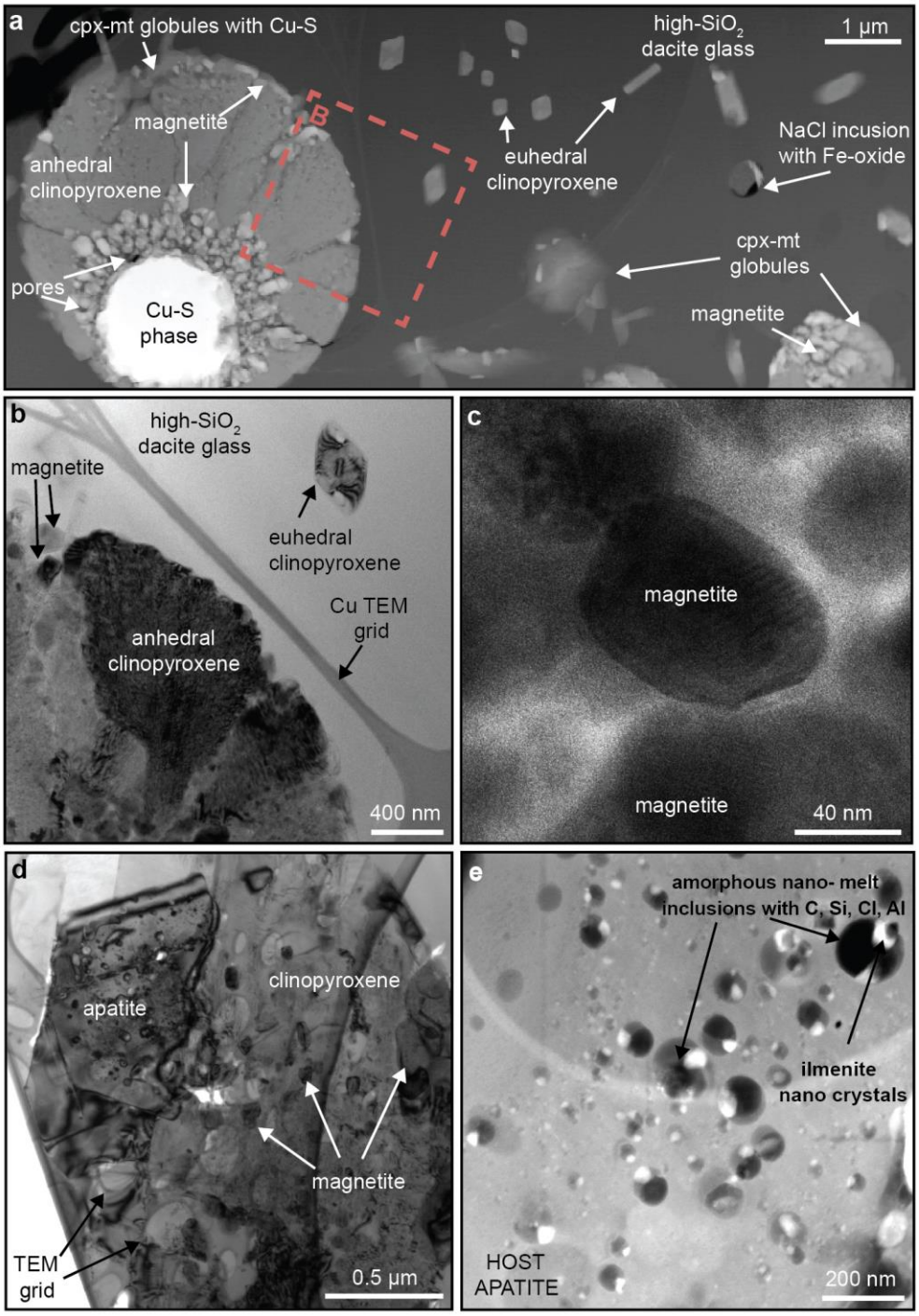

Fig. 3. HR-TEM images of phases in melt inclusions. (**a**) High-angle annular dark field (HAADF) overview image of typical textural relation between conjugate Fe-rich and Si-rich melts: clinopyroxene-magnetite (cpx-mt) globules with occasional Cu-sulfide (digenite) globules embedded in high-SiO_2 dacite glass with euhedral clinopyroxene crystals. (**b**) Bright field (BF)

image of two generations of clinopyroxene crystals. (**c**) BF image of anhedral magnetite hosted in clinopyroxene from cpx-mt globules. (**d**) BF image of subhedral apatite in clinopyroxene-magnetite globule. (**e**) HAADF image of immiscible nano melt inclusions in host apatite from (d).

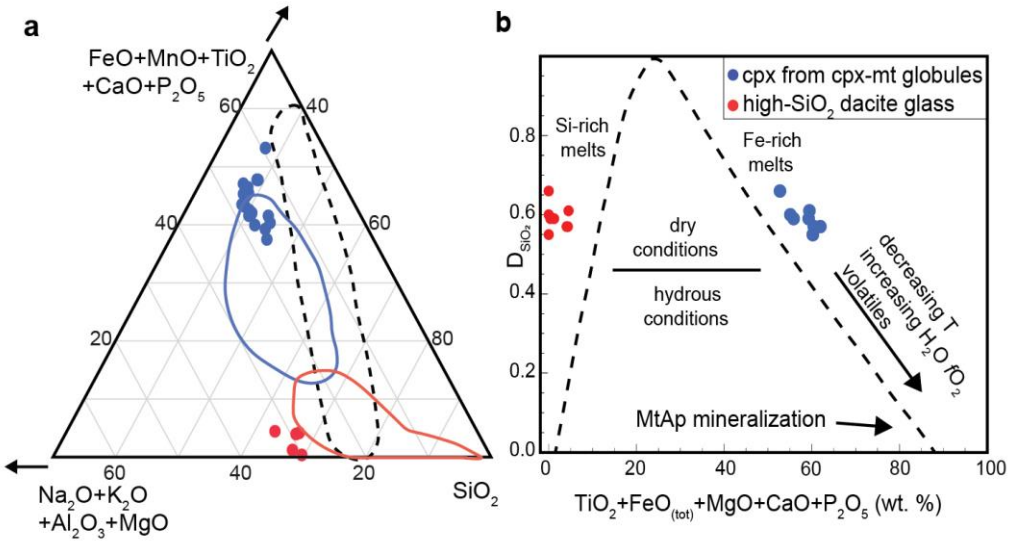

Fig. 4. Chemical composition of Fe-rich and Si-rich melts. (**a**) Ternary plot showing immiscible Fe-rich and Si-rich melts [39] based on FEG-EPMA point analyses (Table S2-3). Note that Fe-rich apex records extremely complex immiscibility. Blue and red fields – previous chemical analyses of melt inclusions in El Laco andesite [17]. Immiscibility fields inside the dashed line were established experimentally [40]. (**b**) Plot of SiO_2 partitioning between the Fe- and Si-rich conjugate melts as a function of elements entering the Fe-rich melt with plotted average composition of conjugate melts in individual melt inclusions from this study (after [23,26]). The dashed line following the conjugate melt pair compositions is based on experimental data on intermediate-composition magmas and tholeiitic systems, and on natural immiscible melt globules [23,26]. See also Fig. S10.

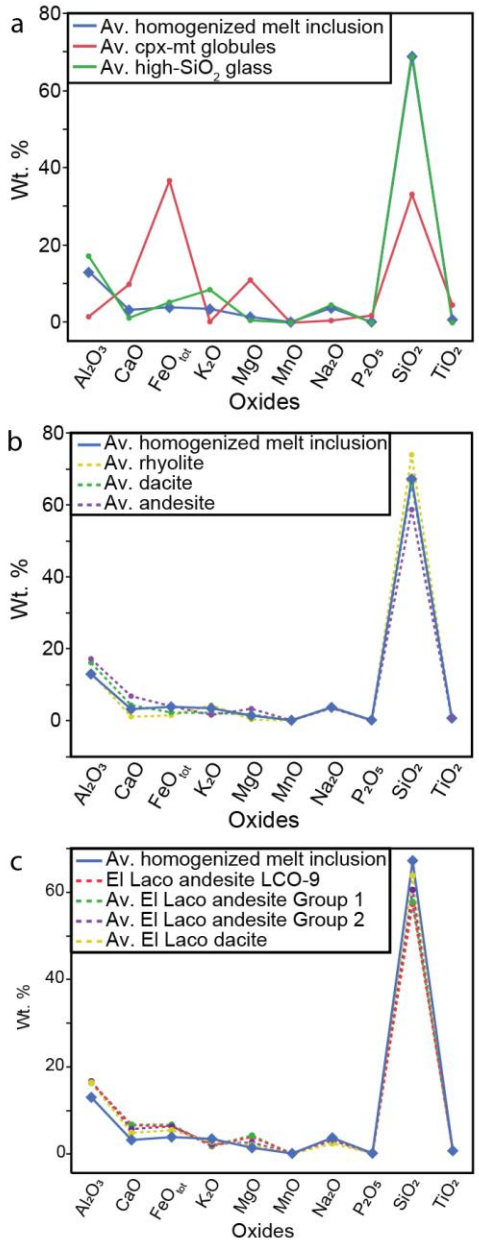

389

390 **Fig. 5. Composition of immiscible Fe-rich and Si-rich melts and parental melt.** The
391 comparison of average composition of homogenized melt inclusions (Table S1) with: (**a**) cpx-mt
392 globules and high-SiO_2 dacite glass from crystallized melt inclusions; (**b**) examples of volcanic
393 rocks [41]; (**c**) average compositions of El Laco host rocks samples [14] and whole rock LCO-9
394 sample hosting immiscible melt inclusions from this study (Table S12). See also Fig. S11.

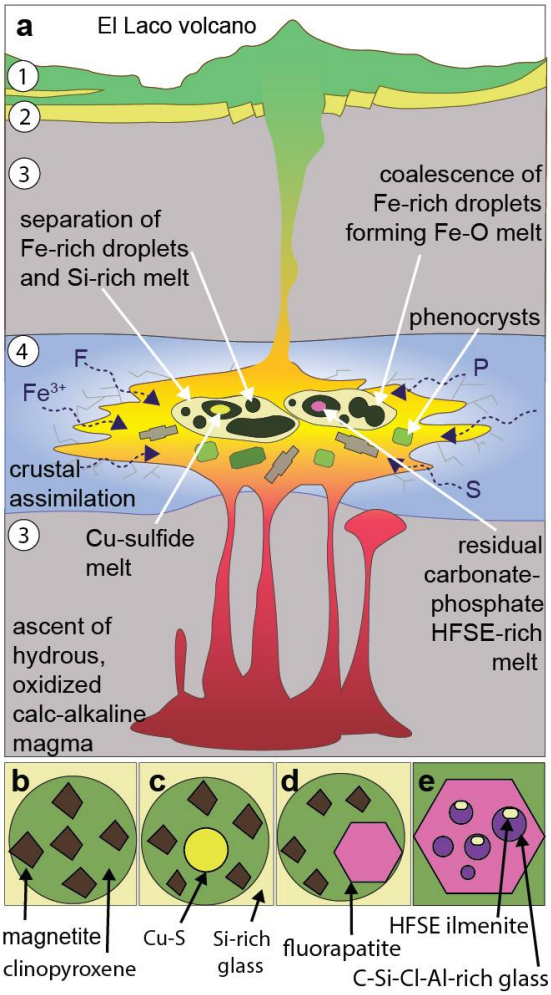

Fig. 6. The genesis of the El Laco MtAp deposit. (**a**) Model of complex separation of multiple immiscible melts in the El Laco andesitic magma chamber. (**b-d**) Drawings of typical mineral phases in globules embedded in Si-rich dacitic glass hosted by immiscible melt inclusions found in this study. (**e**) Drawing of immiscible nano melt inclusions in fluorapatite from (d). Drawings are not to scale. Abbreviations: 1 – El Laco andesitic volcano, 2 - ignimbrites, 3 – underlying crust, 4 - predominantly sedimentary rocks.

Methods

Materials

The samples of unaltered andesite hosting melt inclusions used in this study (LCO-1, LCO-9, and LAC-AND) were collected from Laco Sur and the east flanks of the ELVC (Fig. 1B). Melt inclusions hosted by plagioclase phenocrysts chosen for this study (Fig. S1) show evidence for immiscibility between Fe-rich and Si-rich melts – Fe-rich spherical globules entrained in high-SiO_2 dacite glass - Type 1 melt inclusions, based on categorization by[1]. For more information on other melt inclusion types as well as detailed petrographic study of plagioclase and andesite hosting immiscible melt inclusions, the reader is referred to the aforementioned study. Thin sections were investigated using an Olympus BX-50 transmitted light microscope at Memorial University of Newfoundland (MUN), St. John's, Canada. Melt inclusions were chosen using the general methodology for melt inclusions study[2,3]. Thin sections were further analyzed using a JEOL-JSM 7100F field emission gun scanning electron microscope (FEG-SEM) with back-scattered electron (BSE) imaging capabilities under a 15kV rating voltage at MUN.

High-Resolution-Transmission electron microscope (HR-TEM)

For the HR-TEM investigation, foils with approximately 15 x 7 x 0.15 μm dimensions were cut from the thin sections of the three samples mentioned above by focused ion beam (FIB) milling under ultra-high vacuum conditions using a FEI FIB200 instrument at the GeoForschungsZentrum Potsdam. The extracted foils were placed on a perforated copper grid, and analyzed using an FEI Tecnai G2 F20 X-Twin TEM at the GeoForschungsZentrum (GFZ) Helmholtz Centre, Potsdam, Germany.

426 The TEM was operated at 200 keV with a field emission gun as the electron source. High-
427 angle annular dark-field (HAADF) images were acquired as Z-contrast images (camera length 75
428 mm) or Z-contrast + diffraction contrast images (camera length 220 mm) using a Fishione
429 detector system. Bright- and dark-field images as well as high-resolution lattice fringe images
430 were acquired as energy filtered images applying a 20 eV window to the primary electron beam.
431 The system used was a Gatan Tridiem energy filter (GIF). Electron energy loss (EEL) spectra
432 were acquired in diffraction mode. Ten spectra were acquired with an acquisition time of 1
433 second each. Analytical electron microscopy (AEM) was done using an EDAX X-ray analyser
434 with an ultrathin window. The spectra were acquired in the scanning transmission mode scanning
435 the electron beam within a preselected window thus minimizing mass loss during electron
436 sputtering. The AEM acquisition time was usually for 60 seconds.

437

438 **Field emission gun electron probe micro-analyzer (FEG-EPMA)**

439 Melt inclusions that contain the largest cpx-mt globules with the least number of magnetite
440 crystals, and areas within the high-SiO_2 dacite glass not compromised by any daughter crystals,
441 were chosen for in situ FEG-EPMA compositional point analyses.

442 The FEG-EPMA analyses were acquired using a JEOL JXA-8530F Field Emission Gun
443 Electron Microprobe (FEG-EPMA) using five tunable wavelength dispersive spectometers
444 (WDS) located in the Advanced Instrumentation Laboratory at the University of Alaska-
445 Fairbanks. Energy dispersive X-ray (EDX) spectra were collected simultaneously and used to
446 eliminate analyses where the beam spread into adjacent grains. Data were collected and reduced
447 using Probe for EPMA v12.5.9 (probesoftware.com). Mass absorption corrections were made
448 using the attenuation tables[4].

For silicates, X-rays were collected using a 7keV 1nA focused electron beam. We estimate beam interaction volumes of approximately 900 nm (H) by 600 nm (V) based on Monte-Carlo simulations using CASINO (v2.51)[5]. Element migration was severe in spite of using an extremely low beam current and counts were corrected using a linear time-dependent intensity correction function in Probe for EPMA v12.5.9 software. Iron counts were collected from the Fe Ll-η line[6] and backgrounds were modeled as polynomials. The chosen phases were small for the interaction volume which resulted in variable totals (see Supplementary Text in Supplementary information: Comments on FEG-EPMA totals). Standards analyses and conditions of analyses are included in Table S4.

For copper sulfides, X-rays were collected using a 5keV 3nA focused beam. We estimate beam interaction volumes of approximately 300 nm (H) by 200 nm (V) based on Monte-Carlo simulations using CASINO (v2.51). Element migration did not appear to be a problem during the sulfide analyses. Calibration and reference standards of analyses are in Table S8.

Modal percentage and volume calculations of different phases in melt inclusions

To quantify phase proportions of 1) clinopyroxene-magnetite globules (cpx-mt) and high-SiO_2 dacite glass in melt inclusions, 2) magnetite crystals and clinopyroxene in cpx-mt globules, 3) nano-melt inclusions and its host apatite, and 4) Cu-S mineral phases in cpx-mt globules, 10 images each (TEM and BSE images) were selected and analyzed with ImageJ 1.52a[7]. The results of all analyses are reported in Table S5, S6, S9, and S10, respectively.

The given protocol for all conducted image analyses follows an example of Cu-S volume calculations in cpx-mt globules from sample LCO-1_#4796 (Fig. S6; Table S9).

ImageJ 1.52a software allows for the segmentation of the areas of a digital image based on grayscale intensity, converted to a binary image (Fig. S6), and then the calculation of the area occupied by the chosen phase(s).

The area of each phase calculated using ImageJ 1.52a can be represented as a perfect circle. Therefore, the radius of the assumed perfect circle is back-calculated based on the basic formula for the area of a circle. Having the radius of the whole globules and Cu-sulfide, the formula for the volume (V) of the sphere is calculated. The fraction of Cu-sulfide that occupies the whole globules is calculated based on the ratio of Cu-sulfide volume (V_{CuS}) to whole globules volume (V_{WG}) as below for example (sample LCO-1_#4796; Table S9):

$$\%\ Cu\ sulfide = \frac{V_{CuS}}{V_{WG}} * 100, \quad (1)$$

$$\%\ Cu\ sulfide = \frac{2.91}{47.32} * 100 = 6.15\ \%. \quad (2)$$

Microthermometry

For the homogenization heating experiments, doubly-polished wafers (30-150 µm) were prepared from samples LCO-1, LCO-9 and LCO-AND. Phenocrysts of plagioclase and diopside were inspected under transmitted light to identify melt inclusions. Plagioclase phenocrysts in all three samples contained abundant melt inclusions that ranged in size from ~10 to >100 µm. During the subsequent heating experiments, we mainly observed the smaller inclusions, as these were more commonly fully enclosed within the plagioclase host.

Heating experiments were done using a Linkam TS1400XY heating stage mounted on a custom Olympus BX53 microscope at University of Alberta, Canada. We used an initial heating rate of 100 °C/minute up to 900°C, and a heating rate of 20 °C/minute thereafter until the

493 temperature of last melting was reached. We did not attempt to heat further to dissolve the vapor
494 bubble because the heating experiments were conducted at ambient external pressure.

495 Raman analyses of melt inclusions and their contained vapor bubbles were done using a
496 532-nm laser and a Horiba LabRam HR Evolution Raman microscope at University of Alberta,
497 Canada. Laser power was 100 mW at the source, and focusing was done using a 100x objective
498 lens. Spectra of the vapor bubbles were collected using 60 seconds acquisition time and three
499 accumulations.

500 Detailed results of microthermometry and Raman spectroscopy are described in the
501 Supplementary Text section of Supplementary Information.

502

503 **Electron probe micro-analyzer (EPMA) of homogenized melt inclusions**

504 Quenched, glassy inclusions were exposed to the surface by gentle polishing. Subsequently,
505 they were carbon coated and investigated using a JEOL 7100F field emission scanning electron
506 microscope (SEM) with back-scattered electron (BSE) imaging capabilities at 15 kV at MUN.
507 The major and trace elements of homogenized melt inclusions were measured using a JEOL
508 JXA-8230 SuperProbe electron probe microanalyzer (EPMA) at MUN by calculating the
509 average of compositional traverses crossing the melt inclusions. Traverse started in host
510 plagioclase, went through albitized zone, melt inclusion, the albitized zone and ended in host
511 plagioclase (Fig. S9). This methodology was chosen to be able to reliably distinguish the
512 composition of melt inclusions from albitized zone and host plagioclase. Twenty seven melt
513 inclusion from fourteen plagioclase in three samples were analyzed with nineteen melt inclusions
514 having reliable compositions.

515 The EPMA glass analyses followed the modified methodology from [8]. Each of the traverses
516 across the melt inclusions were analyzed two times using two separate element packages as
517 different EPMA conditions were required. The first package included eight major elements: Na,
518 Mg, Al, Si, K, Ca, Mn, and Fe, and accelerating voltage of 15 kV, 2 nA beam current, and 8 µm
519 beam diameter. The second pass on the same traverses across melt inclusions included trace
520 elements: F, P, S, Cl, Ti, and Cu and accelerating voltage of 15 kV, 140 nA beam current, and 8
521 µm beam diameter. The average composition of major elements in traverse across the melt
522 inclusion were used to correct trace elements using ZAF techniques with the JEOL software.
523 Kaersutite, apatite, pyrite, and cuprite standards were analyzed between unknown major and
524 trace elements analyses.
525
526 **References for Methods:**

527 1. Velasco, F., Tornos, F. & Hanchar, J. M. Immiscible iron- and silica-rich melts and
528 magnetite geochemistry at the El Laco volcano (northern Chile): Evidence for a magmatic
529 origin for the magnetite deposits. *Ore Geol. Rev.* **79**, 346–366 (2016).
530 2. Frezzotti, M. Silicate-melt inclusions in magmatic rocks: applications to petrology. *Lithos*
531 **55**, 273–299 (2001).
532 3. Kamenetsky, V. S. Melt inclusion record of magmatic immiscibility in crustal and mantle
533 magmas. In *Melt Inclusions in Plutonic Rocks* (ed. Webster, J. D.), 81–98 (MAC Short
534 Course, Montreal, 2006).
535 4. Chantler, C. T., Olsen, K., Dragoset, R. A., Chang, J., Kishore, A. R., Kotochigova, S. A.,
536 Zucker, D. S. X-Ray Form Factor, Attenuation and Scattering Tables (version 2.1; online)
537 (2005). doi: https://dx.doi.org/10.18434/T4HS32

5. Drouin, D., *et al.* R. CASINO V2.42 - A Fast and Easy-to-use Modeling Tool for Scanning Electron Microscopy and Microanalysis Users. *Scanning* **29,** 92-101 (2007).

6. Gopon, P., Fournelle, J., Sobol, P. E., and Llovet, X. Low-Voltage electron-probe microanalysis of Fe–Si compounds using soft X-Rays. *Microsc. Microanal.* **19,** 1698–1708 (2013).

7. Schneider, C. A., Rasband, W. S., Eliceiri, K. W. NIH Image to ImageJ: 25 years of image Analysis. *Nat. Met.* **9**, 671–675 (2012).

8. Hanchar, J. M., Watson E. B. Zircon saturation thermometry. In *Zircon, v. 53* (eds. Hanchar J. M., Hoskin, P.), 89–112 (Rev. Mineral. Geochem., 2003).

Supplementary Files

This is a list of supplementary files associated with this preprint. Click to download.

- PietruszkaetalSupplementaryInformationRS1022.pdf